Acta Pharmaceutica Sinica B 2025;15(4):2059−2076

Chinese Pharmaceutical Association
Institute of Materia Medica, Chinese Academy of Medical Sciences

Acta Pharmaceutica Sinica B

www.elsevier.com/locate/apsb
www.sciencedirect.com

ORIGINAL ARTICLE

Taxifolin attenuates liver fibrosis by regulating the phosphorylation of NDRG1 at Thr328 *via* hepatocyte-stellate cell cross talk

Chuan Ding[a,b,†], Zeping Wang[b,†], Kao Shi[b,†], Sunan Li[b], Xinyue Dou[b], Yan Ning[b], Gang Cheng[b], Qiao Yang[b], Xianan Sang[b], Mengyun Peng[b], Qiang Lyu[b], Lu Wang[b], Xin Han[a,b,*], Gang Cao[a,b,*]

[a]*The First Affiliated Hospital of Zhejiang Chinese Medical University, Hangzhou 310000, China*
[b]*School of Pharmacy, Zhejiang Chinese Medical University, Hangzhou 310053, China*

Received 4 July 2024; received in revised form 29 December 2024; accepted 3 January 2025

KEY WORDS

Taxifolin;
Liver fibrosis;
pNDRG1$_{T328}$;
Hepatocyte;
Liver injury;
HSCs;
Cross-talk;
Proteomics

Abstract Taxifolin (TAX) is a natural compound known for its liver protection effect, but the mechanism remains unknown. Phosphorylated proteomics analyses discovered that the phosphorylation level of NDRG1 at T328 was a key event of TAX-improved liver fibrosis. We established models with NDRG1 knockout (KO) *in vivo* and *in vitro,* demonstrating that NDRG1 KO attenuated the development of hepatocyte injury, and combining NDRG1 KO and TAX administration did not result in a reduction in protection against liver injury. Cellular thermal shift assay and surface plasma resonance analysis showed that TAX directly binds to NDRG1 rather than its upstream kinase, subsequently demonstrating that TAX regulated phosphorylation of NDRG1 at T328 through binding to its C289 site. NDRG1 T328A (phosphorylated mutation) and T328E (mimic phosphorylation) *in vivo* and *in vitro* confirmed that pNDRG1$_{T328}$ exacerbates hepatocyte injury along with DNA damage, inflammatory response, and apoptosis, thereby contributing to hepatic stellate cells (HSCs) activation. In contrast, TAX can inhibit the above pathological abnormalities and block hepatocyte injury-triggered HSCs activation and fibrosis. Overall, TAX is a potent liver protection drug primarily targeting NDRG1 and inhibiting pNDRG1$_{T328}$ in hepatocytes.

*Corresponding authors.
E-mail addresses: xinhan@zcmu.edu.cn (Xin Han), caogang33@163.com (Gang Cao).
†These authors made equal contributions to this work.
Peer review under the responsibility of Chinese Pharmaceutical Association and Institute of Materia Medica, Chinese Academy of Medical Sciences.

https://doi.org/10.1016/j.apsb.2025.02.017

1. Introduction

Liver fibrosis, characterized by extracellular matrix buildup, is a reversible wound-healing response to liver injury[1-3]. If not treated, it significantly contributes to long-term morbidity and mortality in patients with chronic liver diseases, such as cirrhosis or hepatocellular carcinoma[4]. Research into pathophysiological factors underlying liver fibrosis has advanced, mainly related mechanisms and signaling pathways[5,6], but has not been fully translated into treatments. Moreover, few drugs for liver fibrosis have been approved by the Food and Drug Administration. Therefore, novel therapeutic strategies and adequate drug preparations for liver fibrosis are urgently needed.

Taxifolin (TAX), or dihydroquercetin, is a natural bioflavonoid[7] compound with antioxidative, anti-inflammatory, and hepatoprotective properties[8,9]. It has been used as a dietary supplement because of its pharmacological properties and non-toxicity[10,11]. TAX affects brain activity and alleviates mental fatigue in healthy young people[12]. It has been included in the Food and Drug Administration-approved list and is mainly used as an antiviral agent or liver protective[13]. It can ameliorate hepatocellular injury by inhibiting inflammation and hepatocyte regeneration and modulating the phosphatidylinositol 3-kinase (PI3K)/RAC-beta serine/threonine-protein kinase (AKT) signaling pathway[14]. TAX reduces malondialdehyde levels by increasing the activity of antioxidant enzymes, thus ameliorating CCl_4-induced acute liver injury[15]. TAX has potential therapeutic effects on liver steatosis and even fibrosis induced by obesity[15]. However, few studies on TAX in liver fibrosis have been conducted, and the possible mechanisms underlying the therapeutic effects of TAX on liver fibrosis have not been comprehensively elucidated.

Post-translational modifications (PTM) are processes where chemical adducts covalently bind to the amino acid side chains or C or N terminals of proteins and are often accompanied by changes in protein conformation and properties[16,17]. PTM plays a critical role in regulating various physiological and pathological processes, providing insights into the mechanisms of liver diseases[18]. Phosphorylation, the most common form of PTM in the liver, enables cells to respond quickly to stimuli, regulates signal transduction and subcellular activity effectively, and stabilizes a range of vital substrates[19]. During phosphorylation, interactions between kinases and phosphatases lead to rapidly adding and removing phosphates, facilitating precise control over signaling events[20,21]. N-myc downstream regulated 1 (NDRG1) belongs to the NDRG family, is a substrate of the kinase serum/glucocorticoid regulated kinase 1 (SGK1), and its expression is upregulated by a stress response[22]. Unlike other NDRG proteins, NDRG1 has a unique three-tandem (GTRSRSHTSE) repeat sequence with a phosphophosphoramic acid attachment site near its C terminal[23]. Its phosphorylation, including Thr346/356/366/328, is critical in multiple physiological functions[24-26]. NDRG1 knockdown can attenuate the expression of adhesion molecules and cytokines induced by interleukin-1β and tumor necrosis factor-α. Hence, NDRG1 is a potential target for alleviating inflammatory responses[27]. Therefore, exploring the sites of NDRG1 phosphorylation and its mechanisms is crucial for managing inflammation-related diseases. Whether phosphorylation modifications are involved in the anti-fibrosis effect of TAX is unclear.

In the present study, we used phosphorylated proteomics combined with a 4D label-free proteomics technology to screen differentially expressed phosphorylated proteins and their sites in our established liver fibrosis mice with TAX intervention. We found that $pNDRG1_{T328}$, rather than Thr346/356/366, was significantly elevated in liver fibrosis and inhibited after TAX administration. Due to these, we identified $pNDRG1_{T328}$ as a core event of TAX-improved liver fibrosis. However, the phosphorylation of NDRG1 at Thr 328 and its mediated activity in diseases, especially liver fibrosis, has been little studied. The present study preliminary found that $pNDRG1_{T328}$ enhanced NDRG1 activity, and TAX intervention reduced the phosphorylation level of NDRG1. Therefore, starting from the biological process mediated by NDRG1, the present study will explore the role of $pNDRG1_{T328}$ in liver fibrosis and the intervention mechanism of TAX, aiming to propose a novel drug treatment strategy for the liver.

2. Materials and methods

2.1. Reagents and antibodies

TAX was purchased from Chengdu DeSiTe Biological Technology and labeled by biotin in Hwayen Biotechnologies. Recombinant Human Transforming growth factor-β (TGFβ) 1 (100-21) was obtained from PeproTech, and lipopolysaccharide (LPS) was purchased from Sigma−Aldrich. Dulbecco's modified Eagle's medium (DMEM) and fetal bovine serum (FBS) were purchased from GIBCO. Complete protease and PhosSTOP inhibitors were purchased from Roche. Other reagents were purchased from Beyotime Biotechnology.

The following antibodies were used: NOD-like receptor family pyrin domain containing 3 (NLRP3) (cs15101), Akt (cs4691), p-PI3K (cs17366), Caspase1 (cs24232), SGK1 (ab32374), NDRG1 (ab124689), Desmin (ab8592), α-smooth muscle actin (α-SMA) (ab7817), PI3K (67071-1-lg), p-AKT (Ser473) (66444-1-lg), F4/80, Mouse EGF-like module-containing mucin-like hormone receptor-like 1 (F4/80) (28463-1-AP), CollagenI (14695-1-AP), Fibronectin (FN1) (BA1772), Caspase8 (d35G2), TGF-β1 (ab179695), Caspase9 (10380-1-AP), mammalian target of rapamycin (mTOR) (7C10) (cs2983), p-mTOR (PAB36313), Caspase3 (ab179517), SOD2 (24127-1-AP), GAPDH (GB11002), DYKDDDK tag (20543-1-AP), PRKACB (12232-1-AP), AKT2 (17609-1-AP), PRKX (16651-1-AP), PDK1 (ab202468), and HA tag (ab236632). In addition, we synthesized antibodies to the specific phosphorylation of NDRG1 at the Thr328 position at Proteintech for subsequent experiments.

2.2. Animal experiments

Male BALB/c mice (20−22 g, 6−8 weeks) were purchased from Charles River in Zhejiang and housed in the Experimental Animal

Center of Zhejiang Medical University (Hangzhou, China). The environment had a temperature of 22−24 °C, humidity of 40%−60%, and a 12 h light/12 h dark cycle. All the mice had free access to water and food. All animal experiments were approved by the Animal Research Committee of Zhejiang Medical University (No. IACUC-20231016-13).

After adaption, the mice were exposed to one of two different regimens for liver injury modeling. (i) For CCl_4-induced acute liver injury, the mice were randomly divided into six groups (six mice per group): control group, TAX alone groups (100 mg/kg), CCl_4 group, and three CCl_4 plus TAX groups (25, 50, or 100 mg/kg). Specifically, the mice in the TAX groups were treated with TAX for 1 week before CCl_4 injection. The mice in the CCl_4 group were given a single subcutaneous injection of 40% CCl_4 (diluted in olive oil) at a 6 mL/kg dose. The mice in the normal and TAX alone groups received an equal dose of olive oil solution. All the mice were killed 48 h after CCl_4 injection. (ii) For CCl_4-induced chronic liver injury, the mice were randomly divided into six groups (six mice per group): control group, TAX alone groups (100 mg/kg), CCl_4 group, and three CCl_4 plus TAX groups (25, 50, or 100 mg/kg). Briefly, to establish liver fibrosis, the mice in the CCl_4 groups were injected with 40% CCl_4 (diluted in olive oil) intraperitoneally at a dose of 3 mL/kg body weight twice a week for 8 weeks. The mice in the TAX groups were treated with TAX at different doses. The animals were sacrificed 9 h after the last TAX administration. All the mice in the two regimens were treated with carotid artery catheterization under anesthetization with isoflurane, and then blood was collected. Finally, the entire liver was obtained and stored in a refrigerator at −80 °C for subsequent experiments.

Liver-specific NDRG1 KO male mice were obtained using CRISPR/Cas9-based adeno-associated virus-8 (AAV-8; catalog GV487, GeneChem Technologies, sgRNA: CATGCCGATGTC GTGATACGT). The establishment of NDRG1 KO mice was confirmed by PCR or Western blot analysis. For overexpression, NDRG1-KO mice were injected with Ad-NDRG1 (NM_008681.2), Ad-NDRG1 (T328E) (NM_008681), or Ad-NDRG1 (T328A, NM_008681; catalog GV651, GeneChem Technologies) through the tail vein. After recovery, mice were pretreated with TAX (100 mg/kg) for 1 week, followed by a single injection of 40% CCl_4 (diluted in olive oil) at a 6 mL/kg dose. All mice were killed at 48 h after CCl_4 injection with carotid artery catheterization under anesthesia. Finally, blood and liver were collected for subsequent experiments.

2.3. Cell culture and treatment

The 293T cell line was obtained from the American Type Culture Collection. Mouse AML12, rat HSC-T6, and human LX2 cells were obtained from Procell Life Science & Technology Co., Ltd. The cells were cultured in DMEM with 10% FBS and 1% penicillin/streptomycin; AML12 cells were cultured in DMEM-F/12 supplemented with 10% FBS, 40 ng/mL dexamethasone, 1% P/S, and 1% insulin−transferrin−selenium. All the cells were maintained in a humidified incubator with 37 °C and 5% CO_2. For the pharmacodynamic evaluation of TAX, HSC-T6 and human hepatic stellate cells (LX-2) were activated by TGFβ (10 ng/mL), and AML12 cells were induced by LPS (1 μg/mL). All the cells were treated with TAX (5, 25, and 125 μmol/L) for 24 h and pharmacodynamically tested.

To achieve stable NDRG1 KO cell lines, we used CRISPR/Cas9 technology on AML12. Single-guide RNA (sgRNA) with a sequence of ACATGACGTGGACCTCGCTG was designed to target NDRG1 using the CRISPR design tool (http://chopchop.cbu.uib.no/). Specifically, the Cas9-sgRNA plasmids and the packaging vectors psPAX2 and pMD2.G were added to 293T cells using linear polyethylenimine (MW 40,000, Yeasen Biotechnology) according to the manufacturer's protocols. The DNA-lipid complex medium was removed and replaced with a standard medium 6−8 h after transfection. After the virus was harvested at 48 and 72 h, the AML12 cells were treated with virus filtrated with 0.45 mm polybrene (16 μg) for 24 h. For overexpression, the cells transfected with Ad-NDRG1, Ad-NDRG1 (T328E), or Ad-NDRG1 (T328A; catalog GV492, GeneChem Technologies) using lentiviruses together with HiTransG P according to the protocols. All the cells were screened with puromycin (1 μg/mL) for stable NDRG1 KO or overexpression cell lines.

2.4. 4D-label free phospho-proteomics

The livers of normal and fibrosis mice were ultrasonically homogenized using a lysis buffer. After quantification, the protein lysate was treated with trypsin digest and made into peptide fragments. The obtained peptides were enriched, modified, desalted, and vacuum drained for mass spectrometry detection. Specifically, the peptides were dissolved by liquid chromatography. Mobile phase A contained a water solution composed of 0.1% formic acid and 2% acetonitrile and was separated by a NanoElute ultrahigh-performance liquid phase system. Mobile phase B contained 100% acetonitrile and 0.1% formic acid. The liquid phase gradient was as follows: 0−74 min, 2%−22% B; 74−80 min, 22%−35% B; 80−85 min, 35%−80% B; 85−90 min, 80% B. The flow rate was maintained at 450 nL/min. The peptides were separated by the ultrahigh-performance liquid phase system, injected into the Capillary ion source for ionization, and then analyzed by timsTOF Pro mass spectrometry. The ion source voltage was set at 1.75 kV, and the parent ion of the peptide segment and its secondary fragments were detected and analyzed using high-resolution TOF. The secondary mass spectrometry scanning range was set at m/z 400−1500. The parallel cumulative serial fragmentation mode was the data acquisition mode.

2.5. Histological staining and immunofluorescence analyses

Liver samples fixed in 10% neutral formalin were dehydrated and embedded in paraffin, and 5 μm-thick sections were prepared and stained with HE, Masson, and Sirius red after dewaxing and hydration. The sections were finally captured on camera with a Zeiss microscope.

For immunofluorescence, liver samples stored at −80 °C were embedded in the SAKURA Tissue-Tek O.C.T. compound and frozen. The immunofluorescence of tissues or cells was observed according to previous protocols. The samples were fixed with 4% paraformaldehyde, washed with phosphate balanced solution (PBS) three times, permeabilized with 0.3% Triton on ice, and blocked with 5% goat serum. Then, the samples were coincubated with the primary antibody at 4 °C overnight. The sample was washed with PBS and reacted with corresponding secondary antibodies, finally blocked with a DAPI-containing anti-fluorescence quencher, and quantified using Image J.

2.6. Western blotting

The proteins were extracted with RIPA buffer supplemented with 1% phenylmethanesulfonyl fluoride, and protein concentration was determined with a BCA assay kit. The treated proteins were separated by sodium dodecyl sulfate-polyacrylamide gel electrophoresis (SDS-PAGE) and transferred to a polyvinylidene fluoride membrane. The transferred membrane was blocked with 5% nonfat milk powder for 1 h. After blocking, membranes were added and incubated overnight at 4 °C. Then, the membrane was incubated with horseradish peroxidase-conjugated secondary antibody. After washing, the membranes were observed using BeyoECL Moon (Beyotime, Nanjing, China) and imaged by a Tanon-5200 apparatus (Tanon, Shanghai, China). The bands were quantified by ImageJ (from the National Institutes of Health).

2.7. Real-time PCR

Total RNA was extracted from mice by using a TRIzol reagent (Beyotime, Nanjing, China), and total RNA from cells was obtained through FastPure Cell/Tissue Total RNA Isolation Kit V2 (Vazyme, Nanjing, China) under an RNase-free condition. After quantification with NanoDrop, cDNA was synthesized using a cDNA synthesis kit (Yifiexue Biotechnology, Nanjing, China). The RT-PCR experiments were performed on a CFX96 real-time system (Bio-Rad, CA, USA) with MonAmp SYBR Green qPCR SuperMix (Monad, Shanghai, China). A qPCR reaction system was prepared according to the 2 × SYBR Green Fast qPCR Master Mix Kit (Yifiexue Biotechnology, Nanjing, China) and was performed on LightCycler 96 Instrument (Roche, Swiss Confederation). All measured values were normalized with β-actin/GAPDH according to the $2^{-\Delta\Delta CT}$ method. These primers are listed in Supporting Information Table S1.

2.8. Co-immunoprecipitation (CO-IP) and pull down

The cells were lysed for 25 min in ice-cold lysate buffer (P0013; Beyotime) containing a protease inhibitor cocktail (Roche) and Phos-stop (Roche). The lysates were incubated with the specified antibody beads for 8 h at 4 °C and washed three times with NP-40 to remove any remaining insoluble material. Western blotting was used to examine the beads after they were boiled in 2 × loading buffers. Bead-bound proteins from AML12 NDRG1 overexpression mutant cell lysates were separated by SDS-PAGE and visualized by BeyoECL Moon after overnight incubation with biotin or biotin-TAX beads in the absence or presence of unlabeled TAX at 4 °C.

2.9. Targets identification of TAX by small-molecule pull-down

Recombinant human NDRG1 protein (ab87685) was incubated with or without TAX overnight and separated by SDS-PAGE. The gel bands were digested with trypsin, and peptides were extracted. The peptides were lyophilized by vacuum centrifugation, resuspended in 0.1% formic acid-water solution, desalted using Monospin C18 column (GL Sciences, Inc.), and performed on a nano-HPLC chromatography system (NanoElute, Bruker Daltonics) connected to a hybrid trapped ion mobility spectrometry quadrupole time-of-flight mass spectrometer (TIMS-TOF Pro2, Bruker Daltonics) *via* a CaptiveSpray nano-electrospray ion source. The protein-containing band in the gel was excised, subjected to in-gel digestion, and analyzed by LC−MS/MS. For MS analysis, survey full-scan MS spectra (*m*/*z* 100−1700) were obtained in positive electrospray mode. Data were searched against NDRG1 (Uniprot ID: Q92597), and the modification site was determined using Fragpipe (v20.0) for protein or peptide identification.

2.10. In vitro SGK1 kinase activity assay

HA-tagged SGK1 plasmids were purchased from Tsingke (Hangzhou, China) and transfected into 293T cells with Lipofectamine 3000 according to protocols (ThermoFisher Scientific, Rockford, IL, USA). Immunoprecipitation with tag antibody was used to purify NDRG1 and SGK1 from AML12 and 293T cells, respectively. Immunoprecipitated NDRG1-Flag product was incubated with SGK1-HA protein in the kinase buffer (20 mmol/L Tris−HCl, pH 7.5, 5 mmol/L $MgCl_2$, 1 mmol/L EGTA, and 0.03% Brij-35, 0.2 mg/mL BSA) containing 20 μmol/L ATP for 1 h at 30 °C in the absence or presence of TAX. Reactions were terminated by adding 2 × loading buffer and analyzed with Western blot.

2.11. Surface plasmon resonance analysis (SPR)

The interactions of TAX with NDRG1, AKT3, and SGK1 were investigated using SPR (Nicoya Lifescience, Waterloo, Canada). Recombinant NDRG1 and SGK1 were coupled onto a Sensor Chip COOH (Nicoya Lifescience, Waterloo, Canada). To validate the affinity between TAX and SGK1 or AKT3, we injected 0−1 mmol/L TAX to pass over the sensor chip at a constant flow rate of 20 μL/min in the running buffer (1% DMSO PBS). The experiment was conducted at 25 °C, and all concentrations were measured in triplicate. The analysis software used in this experiment is TraceDrawer (Ridgeview Instruments ab, Sweden), and the one-to-one analysis model was used.

2.12. Cellular thermal shift assay (CETSA)

LX-2 cells were resuspended in HBSS solution supplementing a protease inhibitor cocktail (Roche), subjected to three freeze−thaw cycles in liquid nitrogen, and physically lysed. The protein supernatant was incubated and placed with TAX on ice for 3 min; the reaction was set at different temperatures or concentration gradients for 3 min. The protein−TAX mixture was centrifuged at 4 °C at 12,000 rpm with a high-speed centrifuge (18R, Dynamica VELOCITY, AU) for 20 min, and the supernatant was collected for subsequent Western blotting.

2.13. Flow cytometry

Cells were spread in a six-well plate at 3×10^5 cells/mL. After the cells adhered, they were treated with LPS with or without TAX for 24 h, digested with trypsin, centrifuged at 1500 rpm for 5 min, and rinsed with PBS twice. For flow cytometry, the cells were resuspended with binding buffer, reacted with annexin V-FITC at room temperature, protected from light for 15 min, mixed with binding buffer, transferred to the flow cytometry system, and detected by BD flow cytometry within 1 h.

2.14. TdT-mediated dUTP nick end labeling (TUNEL)

Tissue sections were fixed with 4% paraformaldehyde for 45 min. Subsequently, the tissue sections were washed 2 times with PBS or HBSS for 10 min each time. After washing, 0.3% Triton X-100 in

PBS was added and incubated for 5 min at room temperature. Prepare the appropriate amount of TUNEL assay solution according to the ratio of TdT enzyme: fluorescent labeling solution: TUNEL assay solution was evenly mixed at 1:5:10 ratio, 50 μL of TUNEL test solution was added to one sample, and incubated at 37 °C for 60 min away from light. At the end of incubation, the samples were washed 3 times with PBS. Finally, the samples were sealed with an anti-fluorescence quenching sealing solution and observed under a fluorescence microscope. The excitation wavelength of the assay is 550 nm, and the emission wavelength is 570 nm (red fluorescence).

2.15. Computational docking modeling

The structure of NDRG1 (PDB ID: 6ZMM)[28] was obtained from the RCSB Protein Data Bank (https://www.rcsb.org/structure/6ZMM). The protein was prepared using Protein Preparation Wizard in Maestro v11.7. Preparation involved removing water molecules and restrained minimization to generate the lowest energy structure at neutral pH while retaining critical amino acids. TAX was prepared using LigPrep in the Schrodinger suite. The OPLS3 force field was used with the following parameters: generation of all possible ionization states at pH 7.0 ± 2.0, desalting, generation of tautomers for all conformers, and retention of one low-energy conformer. Induced-fit docking of NDRG1 and TAX was performed using Glide v8.0 (SP) and Prime v5.3 in Schrödinger Release 2017-1 Induced Fit Docking (Schrodinger, LLC, NY, USA). A grid box was generated centered on residues Cys289. Missing segments in the NDRG1 structure were modeled with AlphaFold before docking.

2.16. Computational MD simulation

After docking, the protein−ligand complex was solvated in a truncated octahedron box of TIP3P water molecules with a buffer distance of 15 Å. Ionizable residues were protonated at pH 7 using the Protein Preparation Wizard in Maestro. Sodium or chloride counterions were added to neutralize the system. Molecular dynamics simulations were performed for 200 ns using Desmond at a temperature of 300 K and pressure of 1 bar. The OPLS3 force field was applied with a 2 fs time step. Long-range electrostatic interactions were treated with the particle-mesh Ewald method using a cutoff of 9 Å. Bond lengths to hydrogen atoms were constrained with M-SHAKE. Conformations were saved every 100 ps for analysis. Root means square deviation (RMSD) of the protein backbone atoms, and TAX was calculated to assess the equilibration and stability of the simulation. Protein−ligand contacts and hydrogen bonds were analyzed to understand binding interactions throughout the trajectory.

2.17. Transcriptome sequencing: RNA-Seq

T328A-NDRG1-KO AML12 and T328E-NDRG1-KO AML12 cells were plated into 6-cm cell dishes, and the cell culture medium was discarded after the cell confluence reached 80%−90%; the cells were washed twice with PBS, and 1 mL of Trizol lysate was added to each well, and the lysate was collected into 1.5 mL. 5×10^6 cells were required for each group, and three replicates were set up simultaneously. RNA was extracted and quality checked by Majorbio Biotechnology Co. After the quality of RNA passed the test, the library was constructed, and transcriptome sequencing was performed on the machine. Differentially expressed genes were analyzed by DESeq2, differential gene analysis was performed to obtain the differentially expressed genes between the two groups, and the screening thresholds were: $|\log2FC| > =0.585$ & P value < 0.05.

2.18. Statistical analysis

Data were presented as mean ± standard deviation (SD). Students's *t*-test (within two groups) and one-way ANOVA (more than two groups) were performed using GraphPad Prism 7.0. A P of ≤ 0.05 was considered statistically significant.

3. Results

3.1. TAX inhibits the development of liver fibrogenesis

To comprehensively explore the therapeutic effectiveness of TAX against liver fibrosis, we established a mouse model of hepatic fibrosis triggered by CCl_4 (Fig. 1A). Blood chemistry examination revealed that the administration of TAX resulted in a notable decrease in the concentrations of aspartate transaminase, aspartate transaminase, and total bilirubin induced by CCl_4 in mice, hence demonstrating its efficacy in mitigating liver injury (Fig. 1B−D). To comprehensively assess the anti-hepatic fibrosis effect of TAX, we measured the activation indices of the HSCs and the significant proteins associated with collagen deposition (Fig. 1E and F, H−J), which were confirmed *in vitro* (Supporting Information Fig. S1A−S1M). The visual analysis of the liver images revealed that treatment with TAX reduced liver scarring and granularity (Fig. 1G). The liver samples from the fibrosis model were subjected to pathological staining. The amount of produced collagen fibers considerably increased in the H&E-stained samples of the model group. The fibers surrounded the clusters of hepatocytes and formed pseudo-lobar structures, and the hepatocytes exhibited eosinophilic and balloon-like structures. Treatment with TAX alleviated these changes (Fig. 1G). To assess the collagen composition in the liver tissue, we carried out experiments using Masson and Sirius Red staining. The model group revealed massive collagen accumulation, which diminished after TAX treatment (Fig. 1G). Consistent with these findings, immunofluorescence analysis of liver sections showed that TAX significantly reduced the levels of α-SMA and collagen I. This effect was indicated by decreased spots at positive places (Fig. 1G). TAX administration effectively restored the equilibrium of extracellular matrix production during the onset of liver fibrosis.

3.2. Phosphoproteome association with the proteome identifies possible TAX targets for liver fibrogenesis

Phosphoproteomics research is essential for elucidating cellular signaling pathways, disease etiology, and the pivotal role of phosphorylated proteins in biological drug development[29]. We analyzed liver proteins through proteomics using 4D label-free phosphoproteome after normalization (Supporting Information Fig. S2A). Phosphoproteome revealed substantial alterations in the pathophysiology of hepatic fibrosis. Most phosphorylation modifications increased, and the expression of some of these phosphorylations was inhibited by TAX administration (Fig. 2A−D). By comparing phosphorylated proteins and phosphorylation sites, we found that the phosphorylation of NDRG1 at T328, S333, and T346 was significantly increased. The M/N phosphorylation ratio

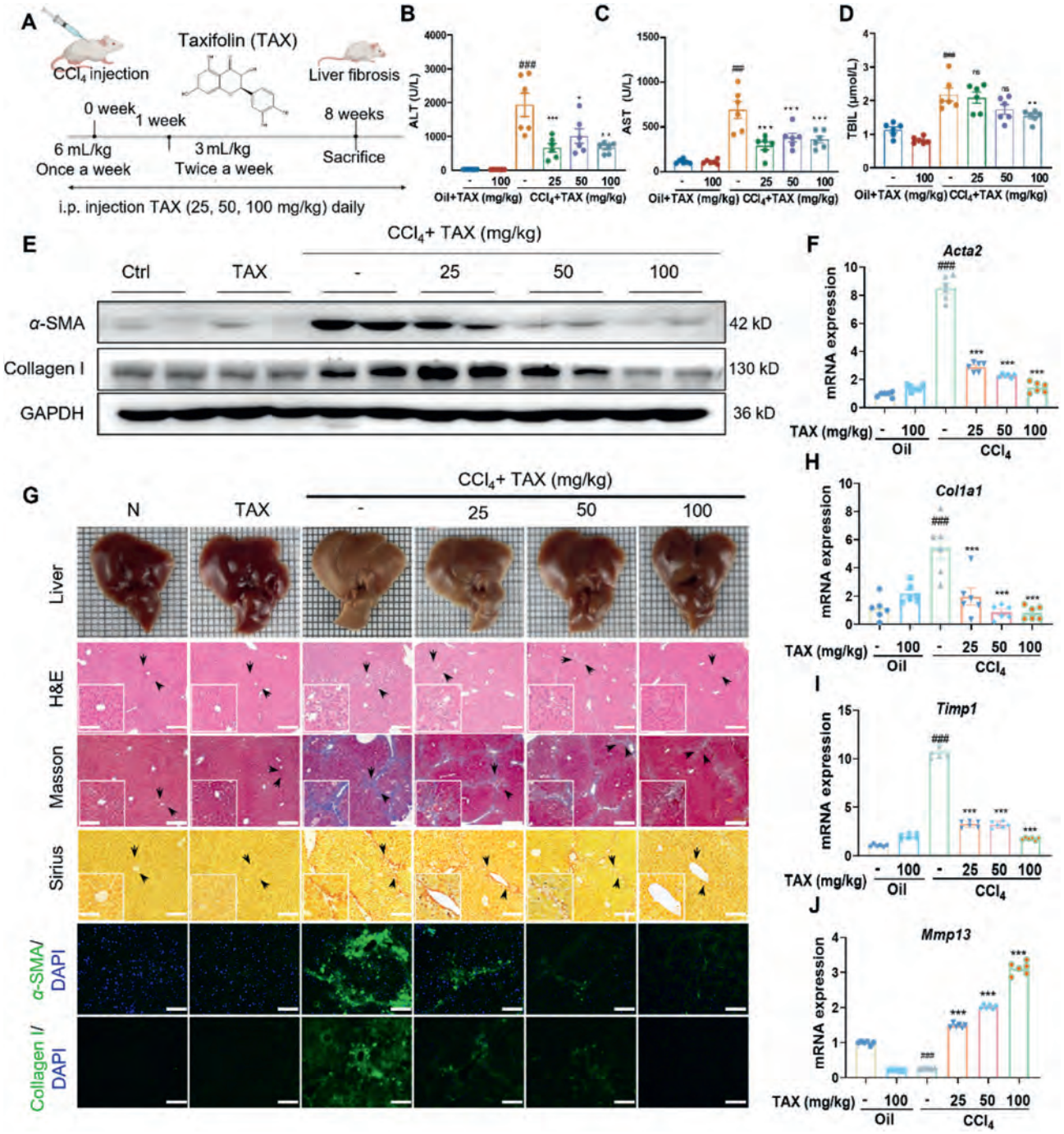

Figure 1 TAX mitigates CCl_4-induced liver fibrosis. (A) Experimental procedure. i.p., intraperitoneal. i.h., subcutaneous. (B−D) The results of serum biochemical indices in mice (including ALT, AST, and TBIL) ($n = 6$ per group). (E) Western blot detected the protein expression levels of α-SMA and collagen I ($n = 3$ per group). (F, and H−J) RT-PCR assessed the mRNA (mRNA) expression levels of *Acta2*, *Col1a1*, *Timp1*, and *Mmp13* ($n = 6$ per group). (G) Liver picture, Scale bar: 1 cm; H&E (Scale bar: 200 μm, Boxes: 40 μm), Masson (Scale bar: 200 μm, Boxes: 40 μm), and Sirius staining (Scale bar: 100 μm, Boxes: 80 μm) of liver tissues. Immunofluorescence analysis for α-SMA and collagen I in the liver tissues (scale bar: 100 μm), $n = 3$−6 per group. Bars indicate the mean ± SD; "$^{\#}$" means N *vs.* CCl_4, $^{\#\#\#}P \leq 0.001$; "*" means CCl_4 *vs.* CCl_4+TAX, $^{*}P \leq 0.05$, $^{**}P \leq 0.01$, $^{***}P \leq 0.001$; "ns" means no significant.

at T328 was 13.41, while the others were 3.332 and 2.151, respectively. At the same time, TAX intervention could significantly inhibit the phosphorylation levels at T328 and has no significant effect on the phosphorylation of NDRG1 at S333 and T346, suggesting that pNDRG1T328 may be a core event of TAX-improved liver fibrosis ($pNDRG1_{T328}$; Fig. 2D−F) (Supporting Information Table S2). To clarify the regulatory effect of TAX on $pNDRG1_{T328}$, we analyzed the proteomic and phosphorylated proteomic data after the administration of TAX. The results indicated that TAX inhibited the expression of this site (Fig. 2E), indicating that the phosphorylation of $pNDRG1_{T328}$ is involved in the pathogenesis of hepatic fibrogenesis and TAX

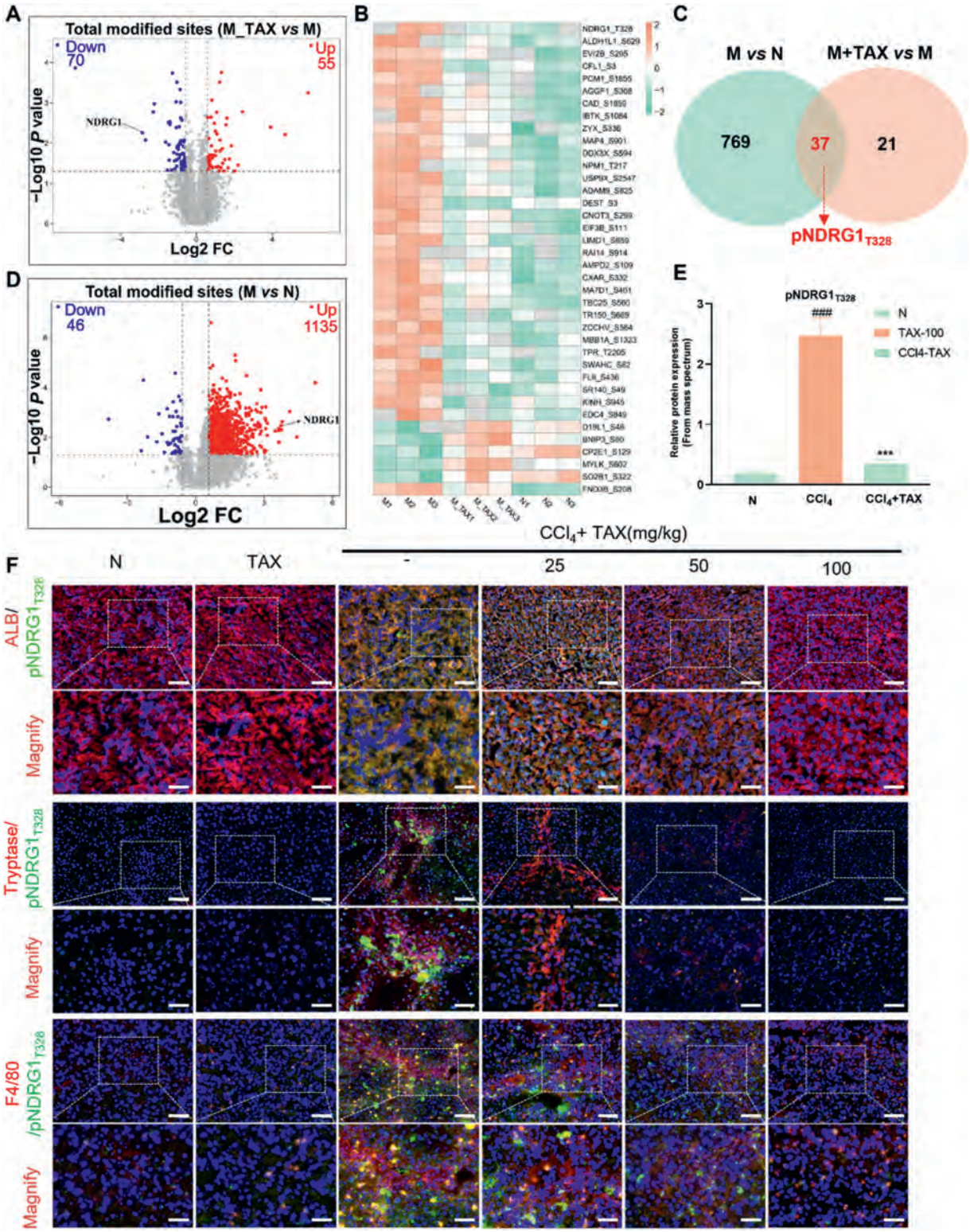

Figure 2 Proteome and phosphoproteome reveal the potential mechanism of TAX anti-fibrosis. (A) Volcano plot analysis ($n = 3$ per group). (B) Heatmap analysis ($n = 3$ per group). (C) Venn diagram analysis ($n = 3$ per group). (D) Volcano plot analysis ($n = 3$ per group). (E) pNDRG1$_{T328}$ protein expression levels ($n = 3$ per group). Bars indicate the mean ± SD; "$^{\#}$" means N *vs.* CCl_4, $^{\#\#\#}P \leq 0.001$; "*" means CCl_4 *vs.* CCl_4+TAX, $^{***}P \leq 0.001$; ns, not significant. (F) Cellular localization of pNDRG1$_{T328}$ in hepatocytes (ALB), mast cells (tryptase), and macrophages (F4/80), $n = 3$−6 per group, respectively, Scale bar: 100 μm, Boxes: 40 μm.

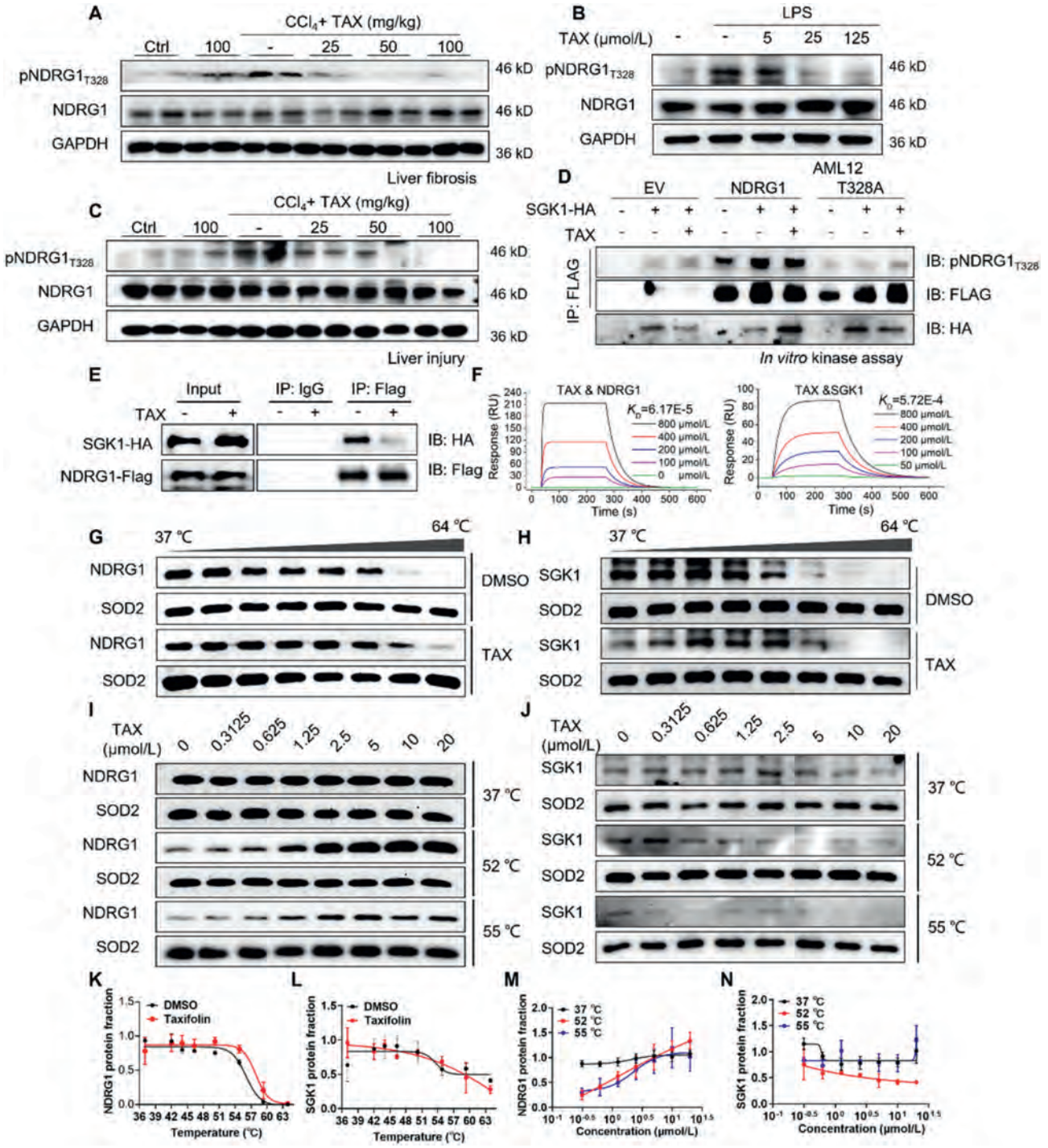

Figure 3 TAX directly targets NDRG1. (A−C) Validation of TAX regulation on pNDRG1 in liver fibrosis/AML12 cells/liver injury models (n = 3 per group). (D) *In vitro* kinase assay (n = 3 per group). (E) CO-IP assay (n = 3 per group). (F) SPR. (G) CETSA evaluated the effect of TAX on the stability of NDRG1 at different temperatures (37−64 °C) (n = 3 per group). (H) CETSA evaluated the effect of TAX on the stability of SGK1 with the temperature increase (37−64 °C) (n = 3 per group). (I) CETSA evaluated the effect of TAX at different concentrations on the stability of NDRG1 at 37, 52 and 55 °C (n = 3 per group). (J) CETSA evaluated the effect of TAX at different concentrations on the stability of SGK1 at 37, 52 and 55 °C (n = 3 per group). (K, L) Hot melt curves based on the relative expression of NDRG1/SGK1 with the increase of temperature (37−64 °C). (M, N) Hot melt curves based on the relative expression of NDRG1/SGK1 treatment with TAX at different concentrations at 37, 52 and 55 °C. The curve was fitted using GraphPad Prism 7.0.

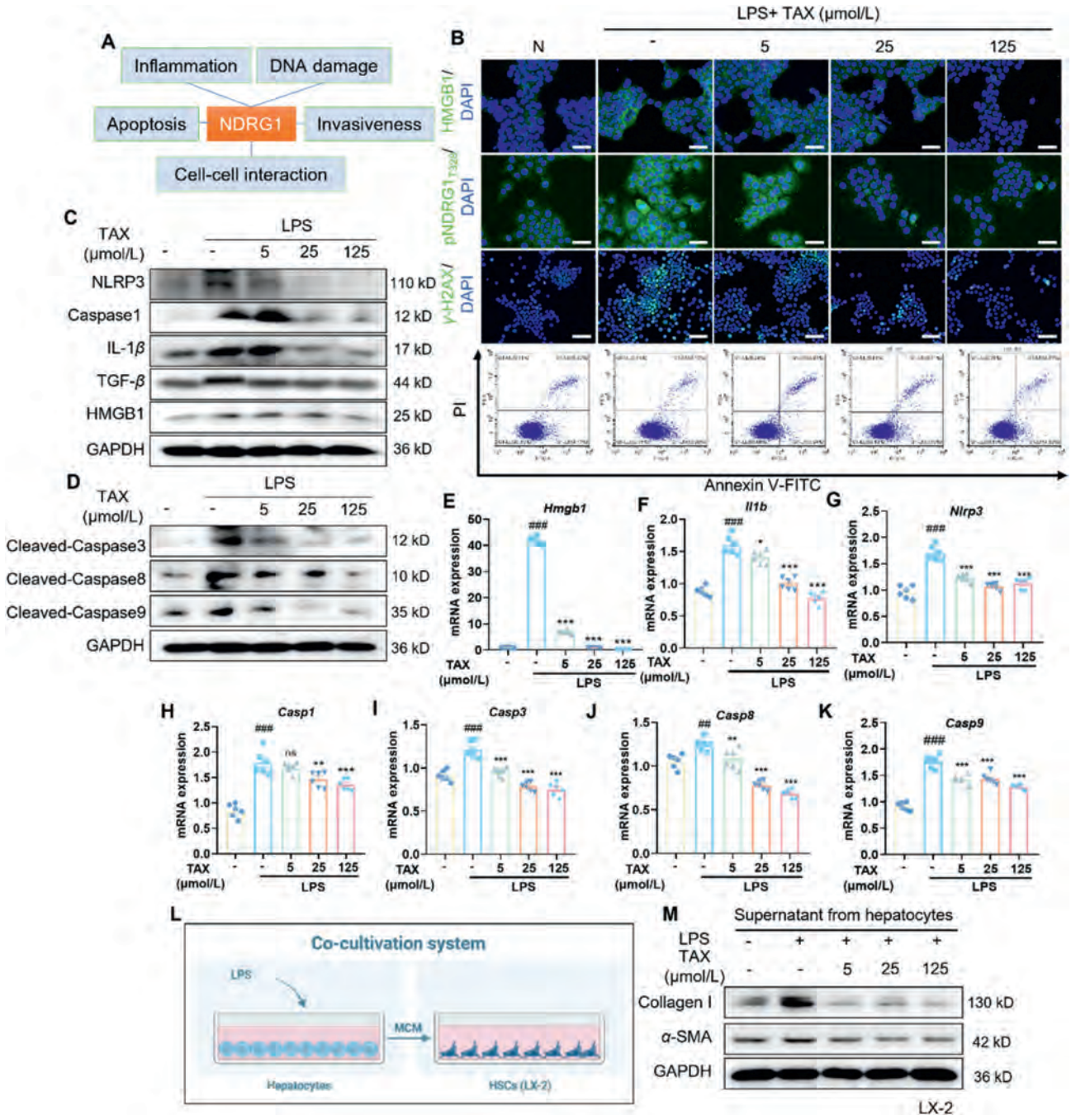

Figure 4 TAX inhibits hepatocytes injury induced HSCs activation. (A) NDRG1 protein-related functions. (B) Immunofluorescence for HMGB1 (Scale bar: 40 μm), pNDRG1$_{T328}$ (Scale bar: 40 μm), and γ-H2AX (Scale bar: 100 μm) and flow cytometry (Scale bar, 20 and 50 μm), $n = 3$−6 per group. (C, D) Western blot detected the expressions of inflammatory factors, HMGB1, and apoptotic factors in damaged hepatocytes ($n = 3$ per group). (E−K) The mRNA expression of inflammatory factors, *Hmgb1*, and apoptotic factors in damaged hepatocytes ($n = 6$ per group). (L) Diagram of co-culture of hepatocytes and hepatic stellate cells. (M) Protein expression of α-SMA and collagen I in LX-2 cells ($n = 3$ per group). Bars indicate the mean ± SD; "$^{\#}$" means N *vs.* LPS, $^{\#\#\#}P \leq 0.001$, $^{\#\#}P \leq 0.01$; "*" means LPS *vs.* LPS + TAX, $^{*}P \leq 0.05$, $^{**}P \leq 0.01$, $^{***}P \leq 0.001$; ns, not significant.

exerts effects against liver fibrosis by targeting this site. Considering that HSCs are key cells in the pathogenesis of liver fibrosis, and their activation is often used as a model of liver fibrosis *in vitro*, we first detected the expressions of NDRG1 and pNDRG1$_{T328}$ in HSCs cells, including mouse hepatic stellate cells (JS-1) and LX-2. We found that these protein expressions were significantly reduced in activated HSCs (Fig. S2B and S2C). To further clarify the function of this site in liver fibrosis, we performed cellular localization of key cells and increased cells involved in the development of liver fibrosis with pNDRG1$_{T328}$. The phosphorylation site was highly localized to the hepatocyte marker albumin (ALB) but weakly localized to macrophages (F4/80) and mast cells (tryptase; Fig. 2F). The expression of pNDRG1$_{T328}$ exhibited gradual reduction upon the administration

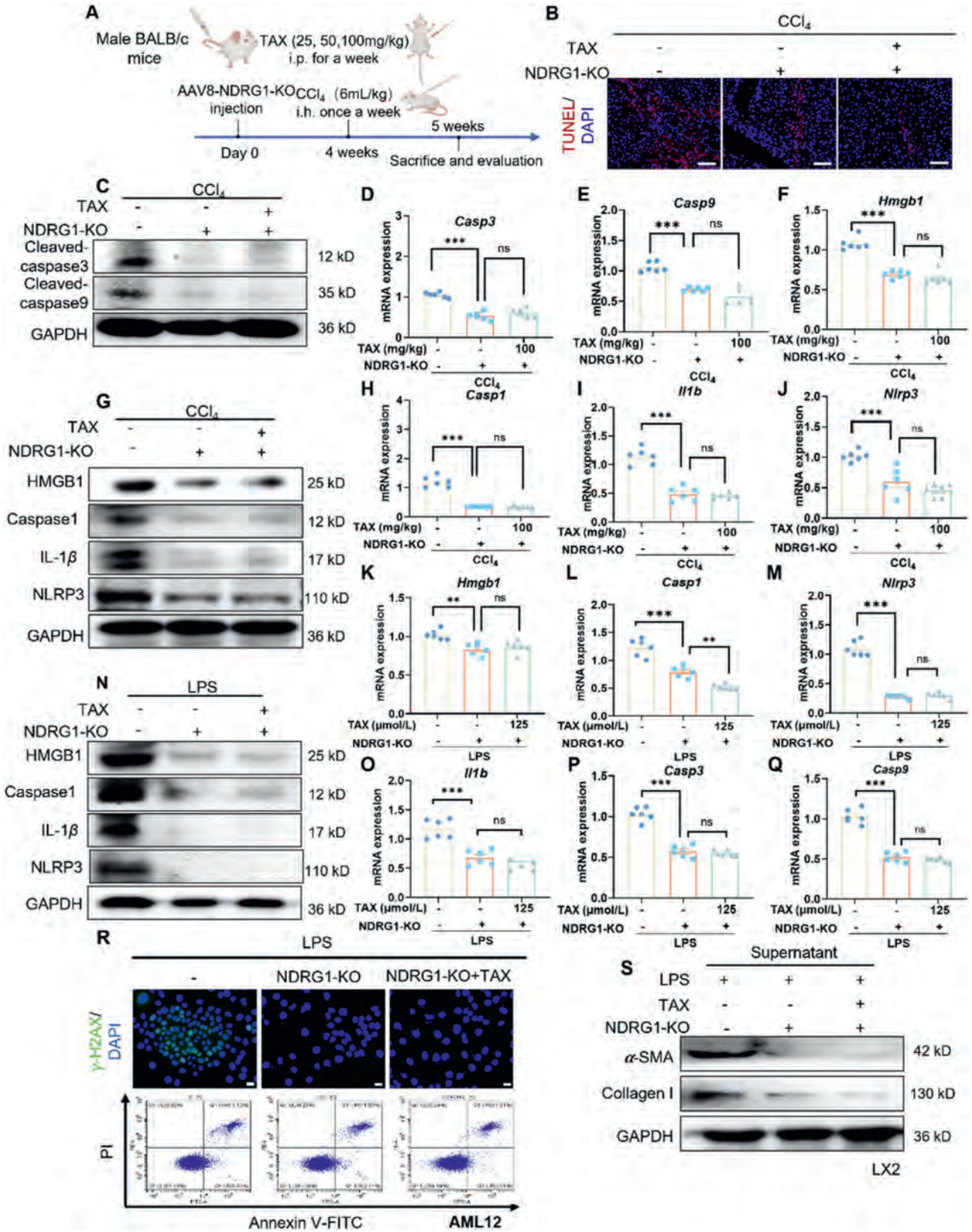

Figure 5 NDRG1 is a potential target for TAX to improve hepatocyte injury-triggered HSCs activation. (A) Experimental procedure. (B) TUNEL stain, Scale bar: 100 μm (n = 3−6 per group). (C) The protein expressions of apoptosis factor in the liver (n = 3 per group). (D−F) mRNA expressions of apoptosis factor in the liver (n = 6 per group). (G) The protein expression of inflammatory factors and HMGB1 in the liver (n = 3 per group). (H−J) mRNA expressions of inflammatory factors and *Hmgb1* in the liver (n = 6 per group). (K−M, O−Q) The mRNA expression of inflammatory factors, *Hmgb1* and apoptotic factors (n = 6 per group). (N) The protein expression of inflammatory factors and

of TAX, consistent with the findings of the phosphoproteomics analysis (Fig. 2F), indicating that $pNDRG1_{T328}$ may be involved in the antifibrotic effect of TAX.

3.3. TAX exerts dephosphorylation by directly targeting NDRG1

We validated $pNDRG1_{T328}$ in the livers of mice with hepatic fibrosis and obtained results consistent with phosphoproteomics, where $pNDRG1_{T328}$ expression was markedly elevated at the onset of hepatic fibrosis. By contrast, the phosphorylation of NDRG1 at the T328 site was inhibited after TAX administration (Fig. 3A). Given that $pNDRG1_{T328}$ was localized in mouse hepatocytes, we selected a mouse hepatocyte cell line (AML12 cells). We stimulated AML12 cells using LPS, a classic hepatocyte-injuried model, to observe the expression of $pNDRG1_{T328}$ with or without TAX administration[30]. The results are presented in Fig. 3B, which indicated an enormous spike in $pNDRG1_{T328}$ level after hepatocyte damage and subsequent inhibition by TAX. To investigate the role of $pNDRG1_{T328}$ in hepatocyte injury, we established a mouse model of acute liver injury (Supporting Information Fig. S3A). Serum biochemical indices and H&E staining showed that intervention with TAX reduced hepatocellular damage and shrunk the lesion area after the onset of acute liver injury (Fig. S3B−S3D). Notably, an abnormal increase in $pNDRG1_{T328}$ level was also demonstrated in the acute liver injury model. After TAX treatment, the expression of this phosphorylation site decreased with the degree of liver injury (Fig. 3C). Considering the relationship between NDRG1 and SGK1, kinase SGK1 was used to verify its phosphorylation and TAX intervention. In the presence of SGK1, NDRG1 phosphorylation was enhanced at the T328 site upon the administration of ATP, suggesting that SGK1 is the upstream kinase of NDRG1 at the T328 site (Fig. 3D). By comparing TAX before and after administration, we found that TAX's role in the regulation of $pNDRG1_{T328}$ is associated with kinase-substrate binding. After TAX administration, the binding of SGK1 to NDRG1 was attenuated, and the phosphorylation of NDRG1 at T328 diminished (Fig. 3D and E). Meanwhile, we found that SGK1 can bind directly to NDRG1, which is the basis for the kinase's function. To clarify how TAX affects the combination of SGK1 and NDRG1, we carried out SPR experiments, indicating that TAX has a strong affinity with NDRG1 (K_D = 6.17e-5) and a weak affinity with SGK1 (K_D = 5.72e-4) (Fig. 3F). These results were verified by CETSA, which showed that TAX can bind to NDRG1, and the bond was more substantial than that between TAX and SGK at different temperatures and in different concentrations (Fig. 3G−N). Moreover, we adopted iGPS1.0 software for predicting kinase-substrate regulations, which, based on RxRxxS/T motif around $NDRG1_{T328}$ and found that AKT3, AKT2, PKACB PRKX and PDK1 can regulate the phosphorylation of NDRG1 at T328 site (Supporting Information Fig. S4A). To further explore the regulation of phosphorylation of NDRG1 by TAX through direct binding to NDRG1, CETSA and SPR were carried out in the present study, showing that TAX can bind to NDRG1 and the bond was more substantial than that between TAX and other kinases of NDRG1 from the results of CEAST as well as SPR (Fig. S4B−S4R). These results showed that NDRG1 is the direct target of the pharmacological effect of TAX.

3.4. TAX regulates NDRG1-mediated biological function in liver fibrosis

To explore whether TAX can target the regulation of NDRG1, we explored whether TAX has a regulatory effect on NDRG1-related biological functions. Literature reviews showed that NDRG1 mainly regulates apoptosis, DNA damage, inflammation, and cell−cell interaction that is closely associated with the development of liver fibrosis (Fig. 4A)[31-33]. Given that the phosphorylation of NDRG1 increases in hepatocyte injury, LPS-induced AML12 cells were used in the present study. The markers of DNA double-strand breaks, gamma H2AX (γ-H2AX), and high-mobility group box-1 protein (HMGB1) consistently increased after the upregulation of NDRG1 phosphorylation at T328. At the same time, these were inhibited after TAX administration (Fig. 4B, C and E, Supporting Information Fig. S5A, S5E and S5F). Immunoblotting results showed that NLRP3 inflammatory vesicle components and caspase-1 spliceosome increased after the maturation and release of IL-1β and upregulation of TGF-β expression during hepatocyte damage. Still, this increase was mitigated by TAX (Fig. 4C−F, G and H). Furthermore, TAX contributed to the inhibition of hepatocyte apoptosis, as indicated by the decreased apoptosis ratio of AML12. The critical proteins involved in apoptosis were downregulated, such as cleaved caspase 3, caspase 8, and caspase 9 in AML12 induced by LPS (Fig. 4B and D, I−K). This effect was mainly manifested by the inhibition of macrophage recruitment, NLRP3 inflammasome activation, caspase1 shear body formation, IL1β maturation, and an increase in TGFβ *in vivo* (Fig. S5A−S5D). HSCs activation induced by the injury of hepatocytes and the release of inflammasome particles is a core event of liver fibrosis. Thus, we collected supernatants from AML12 cells treated with LPS and TAX to stimulate LX-2. The α-SMA and collagen I expression levels in LPS without TAX intervention were significantly higher than in the standard group (Fig. 4L−M). These results indicated that TAX facilitated the cross-talk between hepatocytes and hepatic stellate cells and alleviated liver fibrosis by regulating NDRG1-related biological functions. These results revealed that TAX intervention alleviated inflammation and necrosis, suggesting that TAX can regulate NDRG1-related tasks to a certain extent in fibrosis.

3.5. NDRG1 is a potential target for TAX to improve hepatocyte injury-triggered HSCs activation

To explore the importance of the target NDRG1 for TAX, we established NDRG1 knockout (NDRG1-KO) mutant mice, which were injected with AAV8 *via* the tail vein to induce liver injury (Fig. 5A). We examined the anti-hepatic injury efficiency of TAX after knockdown of NDRG1 by H&E staining and found that TAX's therapeutic effect on liver injury can be eliminated after NDRG1-KO (Supporting Information Fig. S6A−S6C). Moreover, no considerable changes in apoptosis after TAX treatment in the

HMGB1 (n = 3 per group). (R) Immunofluorescence for γ-H2AX (Scale bar: 40 μm) and flow cytometry (n = 3−6 per group). (S) The expressions of α-SMA and collagen I in LX-2 (n = 3 per group). Bars indicate the mean ± SD; "*" means group *vs.* CCl_4−KO, or LPS-KO, $^{**}P \leq 0.01$, $^{***}P \leq 0.001$; ns, not significant.

NDRG1-KO group, which manifested by TUNEL staining and the expressions of factors in caspase cascade reaction, such as caspase3 and caspase9 (Fig. 5B−E). In addition, the knockdown of NDRG1 also weakened the regulatory effect of TAX on the inflammatory response, mainly manifested in the expression and release of inflammatory factors, such as HMGB1, cleaved caspase1, NLRP3, and mature of IL-1β (Fig. 5F−J). Similar results showed that the knockdown of NDRG1 eliminates the sensitivity of hepatocytes to TAX in damaged hepatocytes with NDRG1 KO *in vitro*. Specifically, TAX had little significant effect on injury-related events in AML12, such as DNA damage, apoptotic reaction, and release of inflammatory factors (Fig. 5K−R). To sufficiently explore whether TAX plays an anti-apoptotic role by targeting NDRG1, this study conducted a reverse verification on NDRG1-KO cells that replenishment with NDRG1; that is, NDRG1 was overexpressed in hepatocytes with NDRG1-KO cells. Subsequently, expressions of apoptosis-related factors, such as caspase 3 and caspase 9, were detected, showing that the expression level of apoptosis-related factors in NDRG1-KO hepatocytes was significantly increased after NDRG1 overexpression and up to the level that similar to LPS alone group, while significantly decreased after TAX administration (Fig. S6G and S6H). Given the relationship between injured hepatocytes and activated HSCs, supernatant from NDRG1-KO AML12 cells with LPS and TAX was transferred to HSCs, showing that expression levels of α-SMA and collagen I were increased in the HSCs (LX2), which are the markers for HSCs activation, of note, TAX administration had little effect on hepatic stellate cell activation induced by supernatant, mainly as α-SMA and collagen I had no significant changes compared with the NDRG1-KO group (Fig. 5S), which were verified by NDRG1-KO mutant mice, to be specific, compared to TAX-treated wild-type mice fibrosis, related factors did not further decrease in TAX-treated NDRG1KO mice compared to TAX-treated wild-type mice (Fig. S6D−S6F). These indicated that NDRG1 are potential targets for TAX to improve hepatocytes injury induced HSCs activation, thereby intervening the formation of liver fibrosis.

3.6. TAX inhibits the phosphorylation of NDRG1 at T328 by binding to cysteine 289

To investigate whether NDRG1 is a direct target for TAX to improve liver fibrosis, we performed LC−MS/MS and a pull-down assay (Fig. 6A and B). Specifically, we performed biotin modification on TAX and conjugated it to magnetic beads for Western blot analysis. The results showed that NDRG1 was pulled down by TAX-conjugated magnetic beads rather than TAX and biotin, further confirming that TAX can directly bind to NDRG1 (Fig. 6B). Then, we incubated the NDRG1 recombinant protein in the presence or absence of TAX to LC−MS/MS analysis. Three possible sites on NDRG1 were found for TAX binding: His 63 (H63), Asp189 (D189), and Cys289 (C289) (Supporting Information Fig. S7B−S7E, Fig. 6C and D). The cysteine-containing tryptophan peptide was evaluated and found to have complete information about the b and y ions before and after adding the peptide. The calculated mass of the peptide shown in Fig. 6D was 255.02 Da, which was 152.01 Da greater than that of the peptide MADCGGLPQISQPA, which contains Cys289 and has a calculated mass of 103.01 Da. The mass difference of 152.01 Da perfectly matched that of the TAX cleavage fragment 1 (Fig. S7A). Further, Schrodinger's Induced Fit Docking protocol showed that NDRG1 protein could directly bind to TAX with a docking score of −7.442 kcal/mol. In addition, the chromone ring of TAX occupied a shallow hydrophobic pocket near Cys289 at the interface between the NDRG1 cap and core domains (Fig. 6E, Supporting Information Fig. S8A). Similarly, A 200 ns molecular dynamics simulation of the protein−ligand complex showed that the root-mean-square deviation (RMSD) of the protein backbone atoms showed that both the protein backbone and TAX stabilized after approximately 75 ns, indicating NDRG1 and TAX ligand were calculated over the trajectory to assess equilibration (Fig. 6F), all of which suggesting that TAX may stably bind to NDRG1 by occupying hydrophobic pockets near the domain interface Cys289 and interacting with key amino acid residues such as Gly290, Leu292, Ala287, Leu292, Tyr211, Val207, and Ile295 (Fig. S8B and S8C). This demonstrates the molecular basis for the potential inhibitory activity of cyclopentadiol against NDRG1. Notably, sequence comparison in Fig. 6G showed that the C289 residue in NDRG1 was conserved across species, suggesting that the combination of TAX and NDRG at C289 plays a specific biological function. To verify whether NDRG1 binds to TAX at C289, we induced mutation through the conversion of amino acids at H43, D189, and C289 of NDRG1 to alanine, that is, H43A, D189A, and C289A, respectively, according to a previously described method[34]. Mutant NDRG1 was transfected into AML12 cells, and the corresponding NDRG1 mutant proteins were obtained using CO-IP with Flag. Pull-down experiments of alanine-mutated NDRG1 proteins further supported that TAX covalently modifies C289 but not the H63 and C189 sites of NDRG1 (Fig. 6H). We further investigated whether the C289 mutation affects the inhibitory effect of TAX on phosphorylation at the T328 site of NDRG1. These results were supported by an *in vitro* kinase reaction, showing that only the C289 mutated NDRG1 (C289A) cannot be inhibited by TAX to inhibit the SGK1-induced phosphorylation of NDRG1 at T328 (Fig. 6I). These results suggest that TAX can directly bind to NDRG1 and affect its phosphorylation, especially at T328.

3.7. pNDRG1$_{T328}$ is a core event in TAX-regulated damaged hepatocyte-triggered HSCs activation

To clarify the specific mechanism of TAX on pNDRG1$_{T328}$ and its mediated function in the liver, Ad-NDRG1 (T328E) or Ad-NDRG1 (T328A) that mimics nonphosphorylated mutant and phosphorylation of NDRG1 at T328, respectively, were constructed and injected into NDRG1-KO mice *via* the tail vein (Fig. 7A). After acclimation, the mice received single CCl_4 injections to construct liver injury. Interestingly, there was little significant difference in blood biochemistry between T328A and T328E (Fig. 7B and C). In contrast, the images of the livers and H&E staining showed that compared with the T328A group, the T328E group showed severe liver cell damage, reversed after TAX intervention (Fig. 7D). Of note, T328A and TAX treatment groups showed minor liver damage, and there was no significant difference between them. Compared with T328A, T328E exacerbated inflammatory reactions in the livers of mice, which was mainly manifested by the activation of NLRP3 inflammasome and an increase in HMGB1. At the same time, these effects were ameliorated by TAX administration (Fig. 7E−I), confirmed in AML12 cells with NDRG1 T328A or T328E (Supporting Information Fig. S9A−S9F). To further explore the role of NDRG1 phosphorylation in hepatocyte injury, we used Co-IP technology to explore the proteins that interact with NDRG1 (Supporting Information Fig. S10A). After screening and verification, we found that NDRG1 can interact with

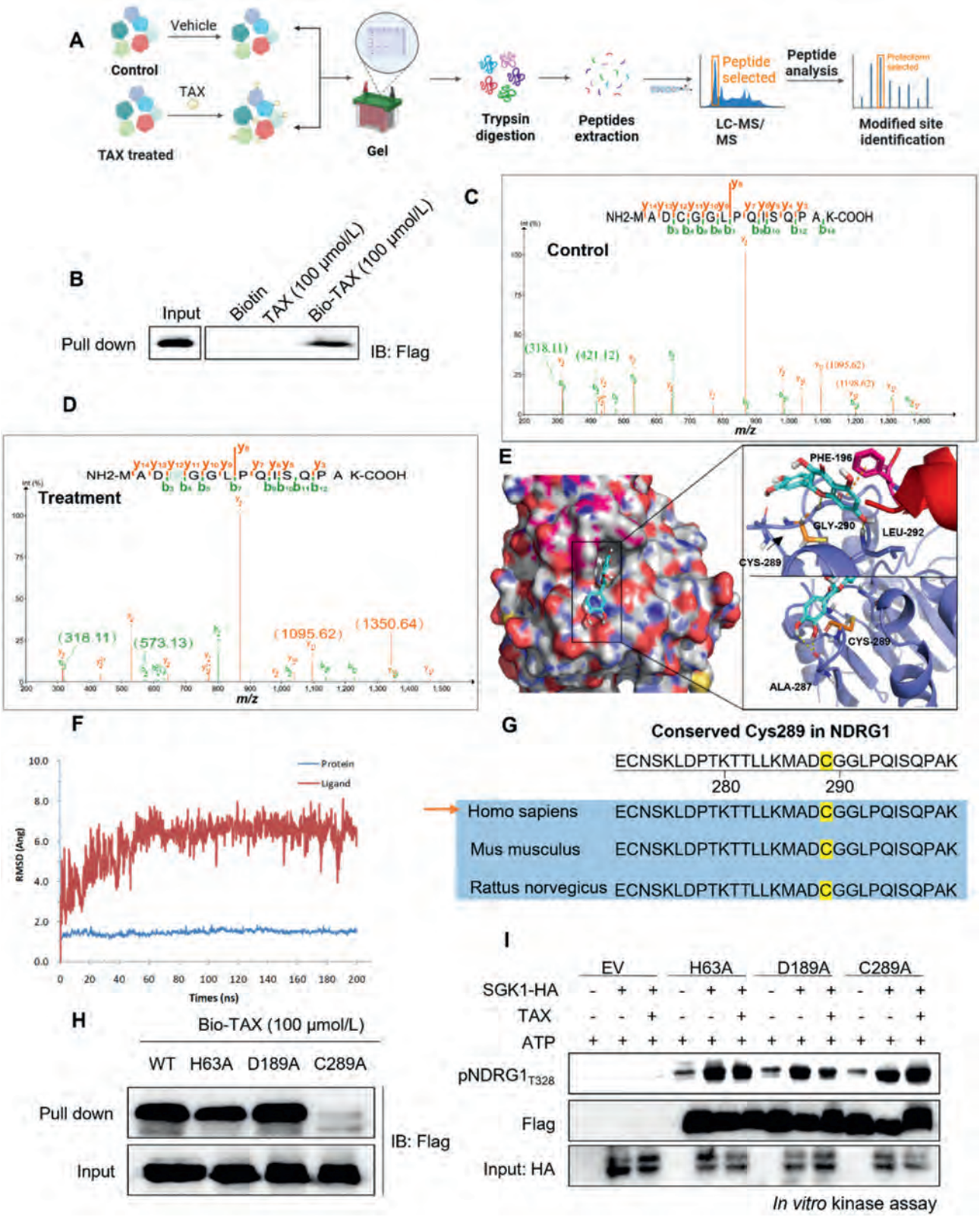

Figure 6 TAX inhibits the phosphorylation of NDRG1 at T328 by binding to cysteine 289. (A) Schematic diagram. (B) Pull down. (C, D) LC−MS/MS analysis. (E) Docking modeling. (F) The root-mean-square deviation (RMSD). (G) A comparative analysis of NDRG1 sequences from various species and isoforms was conducted. (H) Pull down evaluated the combination of Bio-TAX and NDRG1 ($n = 3$ per group). (I) *In vitro* kinase assay detected the effect of SGK1 on NDRG1 phosphorylation ($n = 3$ per group).

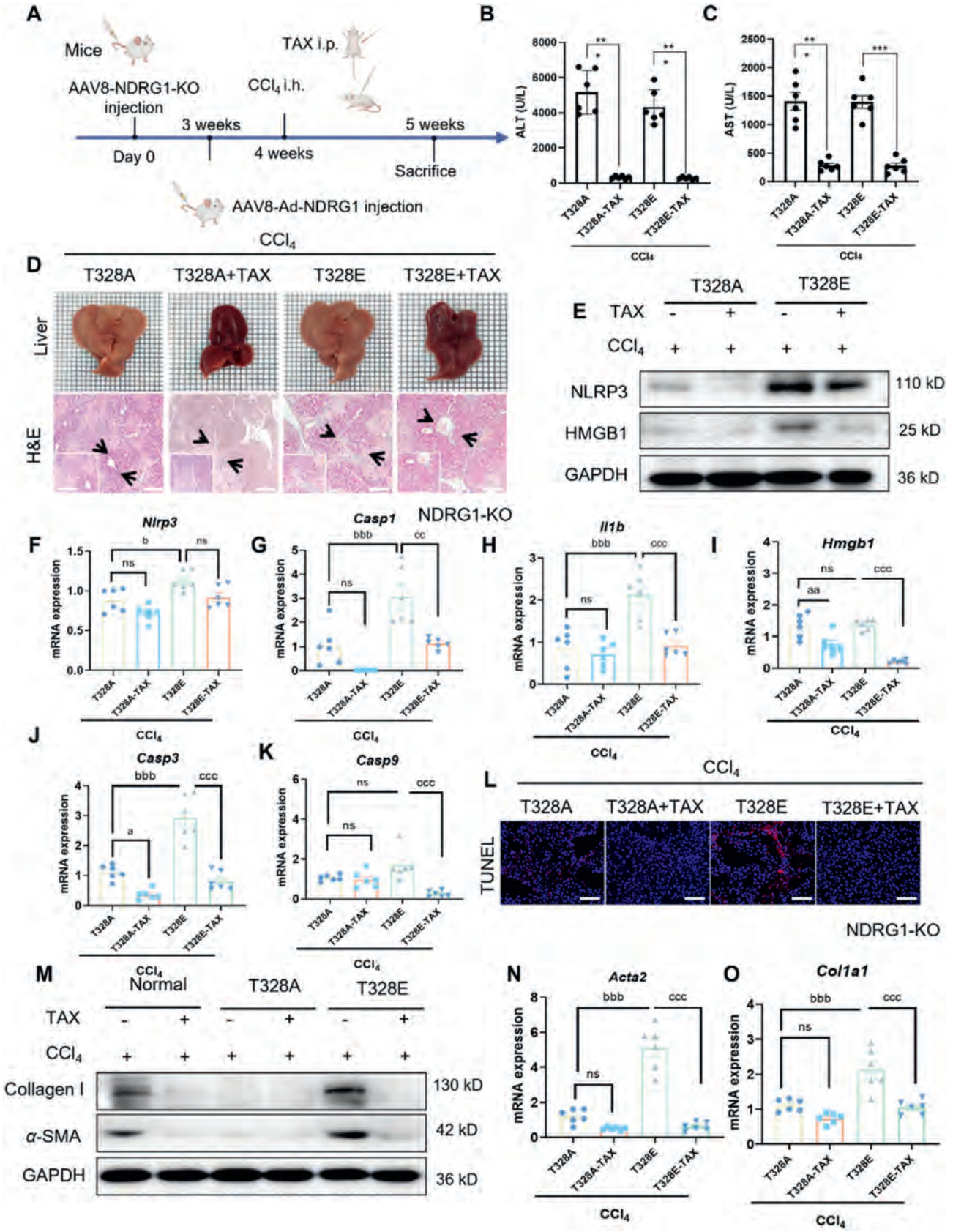

Figure 7 pNDRG1$_{T328}$ is a core event of a TAX-improved liver injury and fibrosis. (A) Experimental procedure. (B, C) Serum biochemical indices (ALT and AST) (n = 6 per group). (D) The gross appearance of livers (Scale bar, 1 cm), H&E staining (n = 6 per group), Scale bar: 200 μm, 40 μm (Boxes). (E) The protein expressions of HMGB1 and NLRP3 in the liver (n = 3 per group). (F−K) The mRNA levels of *Nlrp3*,

calreticulin (CRT), which was confirmed by the results of immunofluorescence and CO-IP (Fig. S10B−S10D). Moreover, overexpression of NDRG1 can lead to increased membrane displacement of CRT, resulting in increased accumulation of calcium ions (Fig. S10E−S10G). Furthermore, NDRG1 phosphorylation (T328E) could increase the interaction between NDRG1 and CRT and the expression of calcium ions. At the same time, these phenomena were not significant in cells with NDRG1 phosphorylation mutation (T328A) (Fig. S10G and S10H). Considering the relationship between CRT-mediated- calcium ion and apoptosis33, we speculated that the mechanism of pNDRG1T328 in liver cell injury might be due to apoptosis caused by calcium overload. Subsequently, the expressions of apoptosis-related indicators in hepatocytes were detected. The results showed that TAX alleviated apoptosis in acute liver injury and hepatocyte exacerbated by T328E (Fig. 7J−L, Fig. S9G−S9J). To explore the role of hepatocyte $pNDRG1_{T328}$ in liver fibrosis, the expressions of fibrotic factors were detected in the present study, showing that the expression levels of α-SMA and collagen I were higher in T328E group than those in the other group and could be reversed by TAX administration (Fig. 7M−O). Of note, compared to TAX-treated mice, T328E (T328E-TAX) overexpression also abolishes TAX-reduced liver fibrosis (Fig. 7M). Given that the presence or absence of NDRG1 can influence damaged hepatocyte triggered HSCs activation, to explore further the role that $pNDRG1_{T328}$ plays in this process, the co-culture system of hepatocytes and HSCs was established *in vitro*, the results showed that the expression levels of α-SMA and collagen I were higher in T328E-NDRG1 KO-AML12 cell supernatant than those in the TAX-treated as well as T328A samples (Fig. S9K). To further explore the exploration and validation of the mechanisms of crosstalk between hepatocytes and HSCs in-depth, we measured the expressions of exosome-related factors in supernatants, including CD63 and CD81, showing that LPS could increase the expressions of CD63 and CD81, which initially confirmed that the crosswise between hepatocytes and HSCs may be carried out by exosomes (Supporting Information Fig. S11A). Moreover, we examined the effect of NDRG1 phosphorylation (T328A and T328E) on the release of exosomes in damaged hepatocytes, which also confirmed that the phosphorylation of NDRG1 (T328E) can enhance the activation of LX2 cells by promoting the formation of exosomes (Fig. S11B), all of these revealed the mechanisms of crosstalk between hepatocytes and HSCs to a certain extent. These suggest that TAX improves HSC activation and fibrosis through its regulation of $pNDRG1_{T328}$ in hepatocytes.

3.8. $pNDRG1_{T328}$-mediated PI3K−AKT−mTOR pathway participates in the amelioration of TAX on liver fibrosis

Although our study explored the role of pNDRGT328 in liver fibrosis, such as inflammation and apoptosis, the precise mechanism by which pNDRG1T328 operates concerning the biological function of NDRG1 remains obscure. Therefore, we collected T328A-NDRG1 KO-AML12 and T328E-NDRG1 KO-AML12 cells for RNA sequencing analysis. A comparative analysis showed increased gene expression in cells after T328A and T328E treatments. These differential genes were enriched in the PI3K−AKT−mTOR pathway (Fig. 8A, Supporting Information Fig. S12A). We first performed PI3K−AKT−mTOR signaling pathway assay for further verification in NDRG1 KO AML12 cells treated with LPS plus T328A or T328E. T328E, as compared with T328A, activated the signaling pathway, and the results were confirmed in NDRG1-KO mice injected with Ad-NDRG1 (T328A or T328E), indicating that $pNDRG_{T328}$ regulates hepatocyte injury about the PI3K−AKT−mTOR pathway (Fig. 8B and C). These changes induced by T328E were reversed by TAX administration *in vivo* and *in vitro*. To further reveal whether the regulatory effect of TAX on the PI3K−AKT−mTOR pathway is related to its binding with NDRG1, we detected the relevant indicators of this pathway in NDRG1-KO mice and AML12 cells. Without NDRG1, the PI3K−AKT−mTOR pathway was inhibited, followed by the regulatory effect of TAX (Fig. 8D and E, Fig. S12B and S12C). Given that $pNDRG1_{T328}$ was screened during liver fibrosis and identified in injured hepatocytes, its role in the mediation of PI3K−AKT−mTOR pathway and regulation of TAX were detected in liver fibrosis and LPS-induced AML 12 cells. We found that the PI3K−AKT−mTOR signaling pathway was activated at the onset of injury and disease and inhibited by TAX *in vivo* and *in vitro*, consistent with the results of TAX-regulated disease cure (Fig. 8F and G). These results supported our hypothesis that TAX inhibits the PI3K−AKT−mTOR signaling pathway by preventing the phosphorylation of NDRG1 at the T328 site, thereby impeding the hepatocyte-hepatic stellate cell crosstalk, ultimately ameliorating liver fibrosis.

4. Discussion

In this study, we established liver injury and liver fibrosis models[35,36] and identified that TAX can be used as a dietary supplement for liver protection. Phosphorylated proteomics combined with protein molecular analysis and *in vivo* functional studies revealed that the mechanism of TAX on liver fibrosis may be the phosphorylation of NDRG1 at T328 and its mediated DNA damage, hepatocyte apoptosis, inhibited release of DAMPs, and activation of HSCs. We further demonstrated that the antifibrotic effect of TAX is closely related to the interaction between damaged hepatocytes and activated hepatic stellate cells by regulating $pNDRG1_{T328}$.

As a stress response gene, NDRG1 is regulated by various pathophysiological stimuli and plays a key role in apoptosis and necrosis[37,38]. However, in the liver, NDRG1 is associated with aggressive tumor behavior and is considered a biomarker for hepatocellular carcinoma metastasis and recurrence and poor prognosis[39,40]. The functional role of NDRG1 in liver fibrosis remains unknown. The present study found for the first time that the phosphorylation of NDRG1 at T328 changes considerably. Owing to the well-known catalysis effect of SGK1 on NDRG1[41], a previous study has reported that SGK1 can phosphorylate NDRG1 at Thr346/356/366[42], while these have little impact on the liver protection of TAX. The present study revealed that the phosphorylation of NDRG1 at T328 was catalyzed by SGK1 and weakened after TAX intervention because TAX directly affected the binding of SGK1 to NDRG1. CETSA and SPR analysis

Casp1, *Il1b*, *Hmgb1*, *Casp3* and *Casp9* in the liver ($n = 6$ per group). (L) TUNEL stain, Scale bar: 100 μm ($n = 3$−6 per group). (M) The protein expressions of α-SMA, collagen I ($n = 3$ per group). (N, O) The mRNA expressions of *Acta2*, *Col1a1* ($n = 6$ per group). Bars indicate the mean ± SD; "[a]" means T328A *vs*. T328A-TAX, $^{a}P \leq 0.05$, $^{aa}P \leq 0.01$; "[b]" means T328A *vs.* T328E, $^{b}P \leq 0.05$, $^{bbb}P \leq 0.001$; "[c]" means T328E *vs.* T328E-TAX, $^{cc}P \leq 0.01$, $^{ccc}P \leq 0.001$; "ns" means no significant.

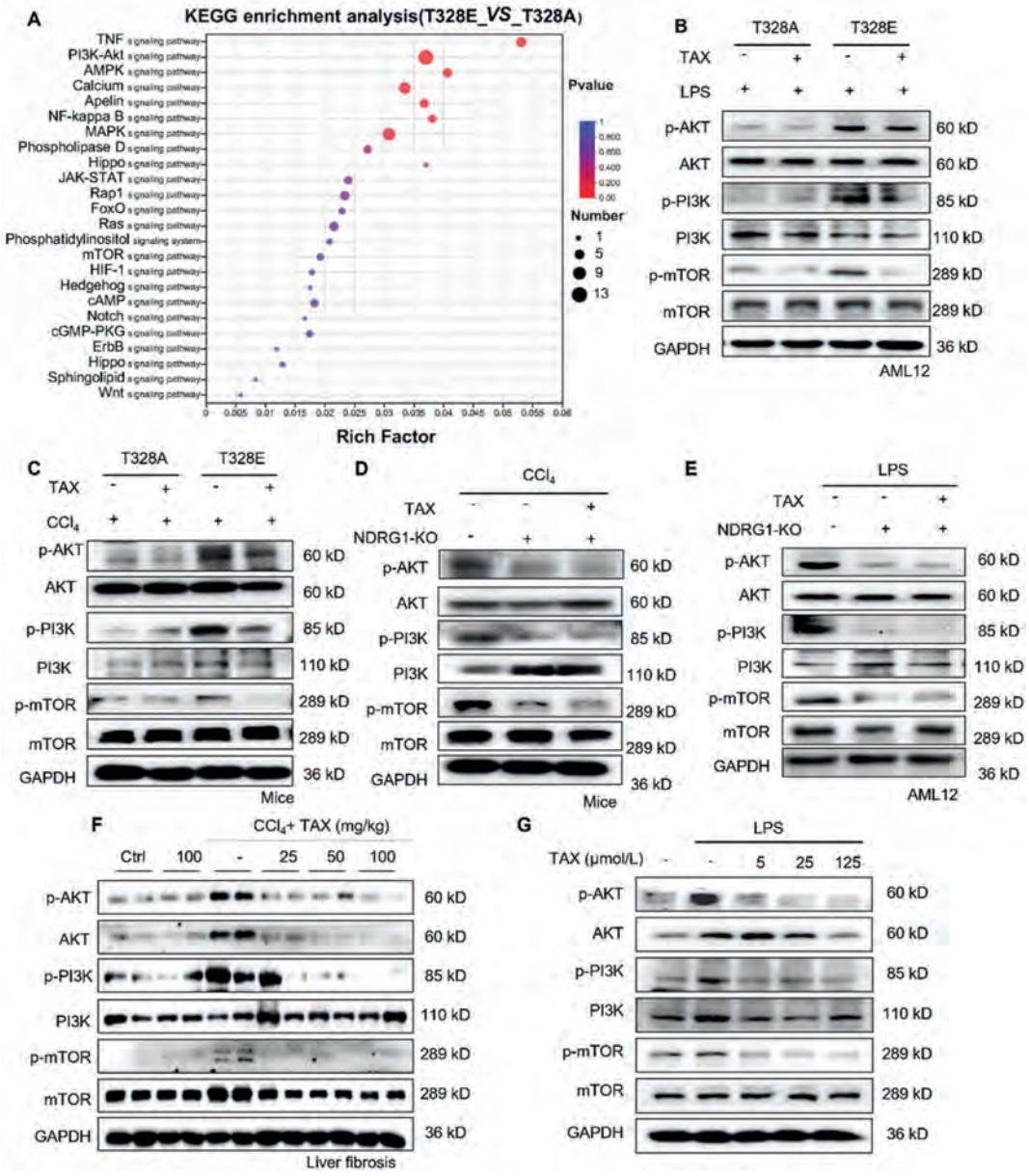

Figure 8 Taxifolin inhibits the pNDRG1$_{T328}$-regulated PI3K−AKT−mTOR signaling pathway. (A) Top enriched pathways. (B−E) The expressions of PI3K−AKT−mTOR pathway related proteins (n = 3 per group). (F) Western blot detected the expressions of the PI3K−AKT−mTOR signaling pathway in CCl_4-induced liver fibrosis mice (n = 3 per group), (G) Western blot detection of TAX on the activation of PI3K−AKT−mTOR signaling pathway in LPS-induced AML12 cells (n = 3 per group).

showed that the binding force of TAX on NDRG1 was more potent than that of its upstream kinase SGK1. Importantly, TAX binding to upstream kinases that may catalyze NDRG1 was weaker than its binding to NDRG1. These data suggest that TAX regulates the phosphorylation of NDRG1 by directly binding to NDRG1 and preventing its association with upstream kinase, thus preventing the phosphorylation of NDRG1.

Liver fibrosis is often accompanied by hepatocyte injury that activates HSCs and is closely related to the biological process mediated by NDRG1[37,43,44]. Hence, to elucidate whether NDRG1 is the direct target of TAX and to improve liver fibrosis, exploring the effects of NDRG1-mediated DNA damage, apoptosis, intercellular interaction, and TAX intervention is critical[45,46]. In addition, it has been shown that apoptosis is closely related to the inflammatory response and that apoptotic factors (including BAK) can target cellular mitochondria to induce programmed cell death, which activates the release of IL-1β from the NLRP3 inflammasome[47]. The current data suggested that although NDRG1 knockout can ameliorate liver tissue lesions to some extent, TAX has little significant effect on hepatocyte injury in the absence of NDRG1. Further studies showed that NDRG1 knockdown inhibited HSC activation induced by hepatocyte damage and weakened the regulation of TAX, indicating that NDRG1 is a target of TAX. This result was further validated in the pull-down assays, leading to an intriguing and emerging question: is the inhibition of TAX on NDRG1 phosphorylation related to different mechanisms or associated with TAX−NDRG1 complex crystal structural biology? Although further studies are needed to

disfigure these mechanisms, the present study verified that TAX binds to the C289 of NDRG1 and thereby reduces the association between NDRG1 and SGK1 and promotes the phosphorylation of NDRG1 being unaffected in the presence of SGK1.

To clarify whether the weakening effect of NDRG1 on TAX liver protection is related to its phosphorylation at T328, we constructed animal and cell models that fully simulated $NDRG1_{T328}$ with or without phosphorylation and implemented TAX intervention. Compared with NDRG1 T328E, overexpression of NDRG1 T328A in NDRG1 KO cells causes little liver injury and weakens the effect of TAX on liver protection. Interestingly, the hepatoprotective effect of TAX was closely associated with the inhibition of hepatocyte injury and consequent HSC activation, which was enhanced by simulated NDRG1 phosphorylation mutation (T328E mutation). Moreover, transcriptomic sequencing revealed that the differential genes of NDRG T328A and T328 E in the liver cells were mainly enriched in the PI3K−AKT−mTOR pathway, which is a classic pathway in liver fibrosis and primarily involved in the occurrence of inflammation and apoptosis. Moreover, the regulatory effect of TAX on $pNDRG1_{T328}$ is also related to the PI3K−AKT−mTOR pathway[48-50]. In general, TAX can affect the phosphorylation of NDRG1, especially T328, and exerts its adverse effects by directly binding to C289 of NDRG1.

In brief, we revealed a crucial role of phosphorylation modification of NDRG1 in the livers of fibrosis mice with TAX intervention. The specific site of NDRG1 phosphorylation Thr328, which participates in hepatocyte injury in liver fibrosis and promotes the activation of HSCs, was first identified. We found that TAX reduced phosphorylation of NDRG1 at Thr328 in the liver and demonstrated that a mutant (T328E) that mimics NDRG1 phosphorylation enhanced the DNA-damaging and apoptotic effects of NDRG1 in hepatocytes. The non-NDRG1 phosphorylated mutant (T328A) inhibited these effects in the hepatocytes. The phosphorylation of NDRG1 at Thr328 significantly increased in the hepatic fibrosis model and was reduced considerably by TAX. The underlying mechanism was that TAX could directly target NDRG1 and inhibit its phosphorylation at Thr328, thereby decreasing its pro-apoptotic effect.

5. Conclusions

In summary, given the vast need for therapeutic targets and drug therapy in liver fibrosis, these findings highlighted that inhibiting phosphorylation at the Thr328 site of NDRG1 in hepatocytes is a potential strategy for TAX in preventing and treating liver fibrosis.

Acknowledgments

The authors gratefully acknowledge the National Natural Science Foundation of China (No. 82104394); "Pioneer" and "Leading Goose" R&D Program of Zhejiang (No. 2024C03102), the Natural Science Foundation of Zhejiang Province (No. LY23H280008, China), and Zhejiang Chinese Medicine University university-level talent special project (No. 2024JKZKTS09, China). We appreciate Tianyang Wang the great support on Methodology, especially cell culture. We also appreciate the great help/technical support/experimental support from the Pharmaceutical Research Center, Academy of Chinese Medical Sciences, Zhejiang Chinese Medical University.

Author contributions

Chuan Ding: Data curation. Zeping Wang: Data curation. Kao Shi: Data curation. Sunan Li: Author contributions, Author contributions; Xinyue Dou: Methodology. Yan Ning: Investigation. Gang Cheng: Software. Qiao Yang: Project administration. Xianan Sang: Investigation; Mengyun Peng: Conceptualization. Qiang Lyu: Software. Lu Wang: Methodology. Xin Han: Writing − review & editing, Writing − original draft, Validation, Funding acquisition. Gang Cao: Writing − review & editing, Validation, Conceptualization.

Conflicts of interest

The authors declare no conflicts of interest.

Appendix A. Supporting information

Supporting information to this article can be found online at https://doi.org/10.1016/j.apsb.2025.02.017.

References

1. Zong Z, Liu J, Wang N, Yang C, Wang Q, Zhang W, et al. Nicotinamide mononucleotide inhibits hepatic stellate cell activation to prevent liver fibrosis *via* promoting PGE2 degradation. *Free Radic Biol Med* 2021;**162**:571−81.
2. Luangmonkong T, Parichatikanond W, Olinga P. Targeting collagen homeostasis for the treatment of liver fibrosis: opportunities and challenges. *Biochem Pharmacol* 2023;**215**:115740.
3. Mahdinloo S, Kiaie SH, Amiri A, Hemmati S, Valizadeh H, Zakeri Milani P. Efficient drug and gene delivery to liver fibrosis: rationale, recent advances, and perspectives. *Acta Pharm Sin B* 2020;**10**:1279−93.
4. Hammerich L, Tacke F. Hepatic inflammatory responses in liver fibrosis. *Nat Rev Gastroenterol Hepatol* 2023;**20**:633−46.
5. Parola M, Pinzani M. Liver fibrosis: pathophysiology, pathogenetic targets and clinical issues. *Mol Aspects Med* 2019;**65**:37−55.
6. Hernandez Gea V, Friedman SL. Pathogenesis of liver fibrosis. *Annu Rev Pathol* 2011;**6**:425−56.
7. Chen S. Biosynthesis of natural products from medicinal plants: challenges, progress and prospects. *Chin Herb Med* 2024;**16**:82−93.
8. Mackie SL, Dejaco C, Appenzeller S, Camellino D, Duftner C, Gonzalez-Chiappe S, et al. British Society for Rheumatology guideline on diagnosis and treatment of giant cell arteritis: executive summary. *Rheumatology* 2020;**59**:487−94.
9. Yan T, Yan N, Wang P, Xia Y, Hao H, Wang G, et al. Herbal drug discovery for the treatment of nonalcoholic fatty liver disease. *Acta Pharm Sin B* 2020;**10**:3−18.
10. Liu Y, Shi X, Tian Y, Zhai S, Liu Y, Xiong Z, et al. An insight into novel therapeutic potentials of taxifolin. *Front Pharmacol* 2023;**14**: 1173855.
11. Liu H, Wang Y, Huang J, Dong Z, Xiao P. Analysis on patents of health care products with substances of medicine food homology in China. *Chin Herb Med* 2024;**16**:412−21.
12. Shinozaki F, Kamei A, Shimada K, Matsuura H, Shibata T, Ikeuchi M, et al. Ingestion of taxifolin-rich foods affects brain activity, mental fatigue, and the whole blood transcriptome in healthy young adults: a randomized, double-blind, placebo-controlled, crossover study. *Food Funct* 2023;**14**:3600−12.
13. Kandeel M, Kitade Y, Almubarak A. Repurposing FDA-approved phytomedicines, natural products, antivirals and cell protectives against SARS-CoV-2 (COVID-19) RNA-dependent RNA polymerase. *PeerJ* 2020;**8**:e10480.
14. Salama SA, Kabel AM. Taxifolin ameliorates iron overload-induced hepatocellular injury: modulating PI3K/AKT and p38 MAPK

signaling, inflammatory response, and hepatocellular regeneration. *Chem Biol Interact* 2020;**330**:109230.
15. Yang CL, Lin YS, Liu KF, Peng WH, Hsu CM. Hepatoprotective mechanisms of taxifolin on carbon tetrachloride-induced acute liver injury in mice. *Nutrients* 2019;**11**:2655.
16. Xiong Q, Chen Z, Ge F. Proteomic analysis of post translational modifications in cyanobacteria. *J Proteomics* 2016;**134**:57−64.
17. Liu R, Li Y, Zheng Q, Ding M, Zhou H, Li X. Epigenetic modification in liver fibrosis: promising therapeutic direction with significant challenges ahead. *Acta Pharm Sin B* 2024;**14**:1009−29.
18. Osna NA, Carter WG, Ganesan M, Kirpich IA, McClain CJ, Petersen DR, et al. Aberrant post-translational protein modifications in the pathogenesis of alcohol-induced liver injury. *World J Gastroenterol* 2016;**22**:6192−200.
19. Inverso D, Shi J, Lee KH, Jakab M, Ben Moshe S, Kulkarni SR, et al. A spatial vascular transcriptomic, proteomic, and phosphoproteomic atlas unveils an angiocrine Tie-Wnt signaling axis in the liver. *Dev Cell* 2021;**56**:1677−93.
20. Pichla M, Sneyers F, Stopa KB, Bultynck G, Kerkhofs M. Dynamic control of mitochondria-associated membranes by kinases and phosphatases in health and disease. *Cell Mol Life Sci* 2021;**78**:6541−56.
21. Zhang J, Yu Z, You G. Insulin-like growth factor 1 modulates the phosphorylation, expression, and activity of organic anion transporter 3 through protein kinase A signaling pathway. *Acta Pharm Sin B* 2020;**10**:186−94.
22. Merlot AM, Porter GM, Sahni S, Lim EG, Peres P, Richardson DR. The metastasis suppressor, NDRG1, differentially modulates the endoplasmic reticulum stress response. *Biochim Biophys Acta, Mol Basis Dis* 2019;**1865**:2094−110.
23. Qu X, Zhai Y, Wei H, Zhang C, Xing G, Yu Y, et al. Characterization and expression of three novel differentiation-related genes belong to the human NDRG gene family. *Mol Cell Biochem* 2002;**229**:35−44.
24. Martinez Lopez N, Mattar P, Toledo M, Bains H, Kalyani M, Aoun ML, et al. mTORC2−NDRG1−CDC42 axis couples fasting to mitochondrial fission. *Nat Cell Biol* 2023;**25**:989−1003.
25. Park KC, Menezes SV, Kalinowski DS, Sahni S, Jansson PJ, Kovacevic Z, et al. Identification of differential phosphorylation and sub-cellular localization of the metastasis suppressor, NDRG1. *Biochim Biophys Acta, Mol Basis Dis* 2018;**1864**:2644−63.
26. Valluri A, Wellman J, McCallister CL, Brown KC, Lawrence L, Russell R, et al. mTOR regulation of N-Myc downstream regulated 1 (NDRG1) phosphorylation in clear cell renal cell carcinoma. *Int J Mol Sci* 2023;**24**:9364.
27. Zhang G, Qin Q, Zhang C, Sun X, Kazama K, Yi B, et al. NDRG1 signaling is essential for endothelial inflammation and vascular remodeling. *Circ Res* 2023;**132**:306−19.
28. Mustonen V, Muruganandam G, Loris R, Kursula P, Ruskamo S. Crystal and solution structure of NDRG1, a membrane-binding protein linked to myelination and tumour suppression. *FEBS J* 2021;**288**:3507−29.
29. Sampadi B, Mullenders LHF, Vrieling H. Phosphoproteomics sample preparation impacts biological interpretation of phosphorylation signaling outcomes. *Cells* 2021;**10**:3407.
30. Zhang Q, Wei J, Liu Z, Huang X, Sun M, Lai W, et al. STING signaling sensing of DRP1-dependent mtDNA release in kupffer cells contributes to lipopolysaccharide-induced liver injury in mice. *Redox Biol* 2022;**54**:102367.
31. Aljobaily N, Viereckl MJ, Hydock DS, Aljobaily H, Wu TY, Busekrus R, et al. Creatine alleviates doxorubicin-induced liver damage by inhibiting liver fibrosis, inflammation, oxidative stress, and cellular senescence. *Nutrients* 2020;**13**:41.
32. Oh YM, Park HB, Shin JH, Lee JE, Park HY, Kho DH, et al. Ndrg1 is a T-cell clonal anergy factor negatively regulated by CD28 costimulation and interleukin-2. *Nat Commun* 2015;**6**:8698.
33. Guo DD, Xie KF, Luo XJ. Hypoxia-induced elevated NDRG1 mediates apoptosis through reprograming mitochondrial fission in HCC. *Gene* 2020;**741**:144552.
34. Ye S, Luo W, Khan ZA, Wu G, Xuan L, Shan P, et al. Celastrol attenuates angiotensin II-induced cardiac remodeling by targeting STAT3. *Circ Res* 2020;**126**:1007−23.
35. Ruart M, Chavarria L, Camprecios G, Suarez Herrera N, Montironi C, Guixe Muntet S, et al. Impaired endothelial autophagy promotes liver fibrosis by aggravating the oxidative stress response during acute liver injury. *J Hepatol* 2019;**70**:458−69.
36. Li Y, Li F, Ding M, Ma Z, Li S, Qu J, et al. Chuanxiong Rhizoma extracts prevent liver fibrosis *via* targeting CTCF−c-MYC−H19 pathway. *Chin Herb Med* 2024;**16**:82−93.
37. Zhao X, Richardson DR. The role of the NDRG1 in the pathogenesis and treatment of breast cancer. *Biochim Biophys Acta Rev Cancer* 2023;**1878**:188871.
38. Park JS, Gabel AM, Kassir P, Kang L, Chowdhary PK, Osei Ntansah A, et al. N-myc downstream regulated gene 1 (ndrg1) functions as a molecular switch for cellular adaptation to hypoxia. *Elife* 2022;**11**:e74031.
39. Yan X, Chua MS, Sun H, So S. N-Myc down-regulated gene 1 mediates proliferation, invasion, and apoptosis of hepatocellular carcinoma cells. *Cancer Lett* 2008;**262**:133−42.
40. Cheng J, Xie HY, Xu X, Wu J, Wei X, Su R, et al. NDRG1 as a biomarker for metastasis, recurrence and of poor prognosis in hepatocellular carcinoma. *Cancer Lett* 2011;**310**:35−45.
41. Sahin P, McCaig C, Jeevahan J, Murray JT, Hainsworth AH. The cell survival kinase SGK1 and its targets FOXO3a and NDRG1 in aged human brain. *Neuropathol Appl Neurobiol* 2013;**39**:623−33.
42. Inglis SK, Gallacher M, Brown SG, McTavish N, Getty J, Husband EM, et al. SGK1 activity in Na^+ absorbing airway epithelial cells monitored by assaying NDRG1-Thr346/356/366 phosphorylation. *Pflugers Arch* 2009;**457**:1287−301.
43. Sun J, Zhang D, Bae DH, Sahni S, Jansson P, Zheng Y, et al. Metastasis suppressor, NDRG1, mediates its activity through signaling pathways and molecular motors. *Carcinogenesis* 2013;**34**:1943−54.
44. Hubel E, Saroha A, Park WJ, Pewzner Jung Y, Lavoie EG, Futerman AH, et al. Sortilin deficiency reduces ductular reaction, hepatocyte apoptosis, and liver fibrosis in cholestatic-induced liver injury. *Am J Pathol* 2017;**187**:122−33.
45. He L, Liu K, Wang X, Chen H, Zhou J, Wu X, et al. NDRG1 disruption alleviates cisplatin/sodium glycididazole-induced DNA damage response and apoptosis in ERCC1-defective lung cancer cells. *Int J Biochem Cell Biol* 2018;**100**:54−60.
46. Luo Q, Wang CQ, Yang LY, Gao XM, Sun HT, Zhang Y, et al. FOXQ1/NDRG1 axis exacerbates hepatocellular carcinoma initiation *via* enhancing crosstalk between fibroblasts and tumor cells. *Cancer Lett* 2018;**417**:21−34.
47. Deo P, Chow SH, Han ML, Speir M, Huang C, Schittenhelm RB, et al. Mitochondrial dysfunction caused by outer membrane vesicles from Gram-negative bacteria activates intrinsic apoptosis and inflammation. *Nat Microbiol* 2020;**5**:1418−27.
48. Wang R, Song F, Li S, Wu B, Gu Y, Yuan Y. Salvianolic acid A attenuates CCl4-induced liver fibrosis by regulating the PI3K/AKT/mTOR, Bcl-2/Bax and caspase-3/cleaved caspase-3 signaling pathways. *Drug Des Devel Ther* 2019;**13**:1889−900.
49. Zhang Z, Shang J, Yang Q, Dai Z, Liang Y, Lai C, et al. Exosomes derived from human adipose mesenchymal stem cells ameliorate hepatic fibrosis by inhibiting PI3K/Akt/mTOR pathway and remodeling choline metabolism. *J Nanobiotechnology* 2023;**21**:29.
50. Liu B, Deng X, Jiang Q, Li G, Zhang J, Zhang N, et al. Scoparone improves hepatic inflammation and autophagy in mice with nonalcoholic steatohepatitis by regulating the ROS/P38/Nrf2 axis and PI3K/AKT/mTOR pathway in macrophages. *Biomed Pharmacother* 2020;**125**:109895.